RSC Advances

ROYAL SOCIETY OF CHEMISTRY

www.rsc.org/advances

AFM-based bivariate morphological discrimination of apoptosis induced by photodynamic therapy using photosensitizer-functionalized gold nanoparticles

Rasoul Al-Majmaie[a,b,c], Eamonn Kennedy[a], Mohamed Al-Rubeai[b], James H. Rice[a], Dominic Zerulla[a*]

[a] School of Physics, University College Dublin, Belfield, Dublin, Ireland

[b] School of Chemical and Bioprocess Engineering, University College Dublin, Ireland

[c] Institute of Laser for Postgraduate Studies, University of Baghdad, Iraq

*Corresponding Author: dominic.zerulla@ucd.ie

Abstract

The apoptosis of cancer cells is linked to characteristic changes in cell properties which include many morphological parameters. Recent studies have indicated that using atomic force microscopy (AFM) to identify mechanical properties of cells at a subcellular scale is an extremely precise way of evaluating the influence of therapies on single cells and subcellular features. This study outlines how apoptosis initiated by photodynamic therapy using photosensitizer conjugated gold nanoparticles mediates the morphological properties of single colon cancer cells, and how these properties can in turn be used as an efficient classifier of cell health. We describe a bivariate statistical classifier of two independent AFM measurements of cell properties (total volume and membrane roughness) which exhibits apoptotic detection accuracy comparable to the prevailing biological standards.

1. Introduction

Apoptosis - the set of highly complex, multi-pathway, multi stage processes which govern programmed cell death - is genetically encoded in all mammalian cells. There has long been considerable interest in developing simple techniques that enable the identification of apoptosis. Typically, the simplest and most direct methods to study apoptosis rely on identifying morphological features associated with cell death. Numerous important morphological hallmarks are known to occur during apoptosis, including nucleic condensation and fragmentation, loss of cell volume, the excretion of intact vesicular structures and changes to membrane roughness.[1-2]

In recent years, many factors have been identified which induce apoptosis. In particular, free-radical mediated cellular damage following oxidative stress has become a central area of study, since the generation of free radicals has been proposed as a universal trigger for the onset of apoptosis.[3,4] Photodynamic therapy (PDT), now an established treatment modality for cancer, capitalizes on the selective generation of free-radical species in malignant cells and therefore efficiently induces cell death. Over the last two decades, the complex pathways which lead to PDT induced apoptosis have been extensively studied. In contrast to other chemical treatments which primarily cause cell death through necrosis, PDT triggers apoptosis via the long-term exposure at low dosage of a photosensitive dye which, after photo-excitation, generates singlet oxygen and free radicals in the cell. Many experimental and treatment parameters are known to influence the efficacy of this process. For instance, the photosensitizer used, dose, light exposure levels, and subcellular localization can all dramatically influence treatment efficacy.[5-8]

Increased understanding of the mechanism of action and the role of these parameters in PDT offers the potential to optimize current PDT protocols. Previous studies have indicated that the detection of mechanical changes on the subcellular scale provides a direct way of evaluating the

influence of PDT on single cells, and the precise role that treatment parameters play in determining the therapeutic outcome.[9,10] Therefore, the determination of ultrastructural changes that occur as a result of apoptosis induced by PDT is of central importance for understanding and gaining new insights into the biomechanics underlying the treatment process.

Traditionally, electron microscopy (EM) has been the most popular method for demonstrating the morphological changes characteristic of apoptosis. It remains the clearest method for determining structure on the nanometer and even sub-nanometer scale.[11] In contrast to EM, atomic force microscopy (AFM) is an emerging, complementary alternative for the investigation of cellular substructures under physiologically relevant conditions. AFM has a diverse range of applications in biology because of its ability to image and resolve features in three dimensions far below the resolution limits of optical microscopy.[12]

The technique employs a small, sensitive tip which is brought into proximity with the cell surface, which generates interaction forces between the tip and sample. In contact mode, the tip is raster scanned over the region of interest, and is deflected with a magnitude proportional to the force interaction at each point with a lateral resolution defined by the tip-sample interaction area. The tip height itself is modulated by a feedback loop which ensures that the tip and cantilever are kept at near constant separation from the sample to avoid tip or surface damage.[13]

So far, AFM research concerning the morphological features associated with apoptosis typically have focused on the measurement of membrane roughness as a function of physiological condition. Somewhat surprisingly, these studies have indicated both large increases[14,15] and large decreases[16,17] in apoptotic cell membrane roughness after various treatments. This discrepancy in apoptotic process associated physiological conditions likely occurs because of the diversity of steps and pathways that can lead to programmed cell death. However, further interrogation and

cross confirmation of these results is urgently needed because, to date, no clear consensus has been established.

To address this, we employed AFM imaging in order to measure the morphological properties of many single cells during apoptosis that was initiated by PDT using photosensitizer-conjugated gold nanoparticles. Despite recent advances in AFM imaging of cell morphology, our observations indicated that no choice of single variables was capable of discriminating apoptosis in the low statistical regime. Therefore, for true mechanical discrimination, a compelling need exists for multivariate morphological analysis, which clearly must be assessed with a larger statistical ensemble. By illustrating a simple bivariate approach based on two independent measurements of cell properties (total volume and membrane roughness) we have shown quite plainly how single variable morphological assessment alone is an unreliable classifier of apoptosis in the low statistical regime, while also demonstrating that the bivariate approach robustly reproduces known viability percentages for larger sample sizes. Our results confirm that under correct experimental conditions and constraints, AFM offers a highly competitive method for determining apoptosis, and is comparable in efficacy to both of the current biological standards for apoptotic detection: fluorescence microscopy and flow cytometry.

2. Materials and Methods

2.1 Synthesis and characterization

Gold nanoparticles (GNPs) were synthesized using the modified Brust-Schiffrin method.[18] PEGylated GNPs were prepared using carboxyl-functionalized PEG (polyethylene glycol) as described previously.[19] Covalent binding of toluidine blue O (TBO) to GNPs was performed using a standard EDC/NHS coupling reaction. The TBO concentration on the surface of the GNPs was measured by comparison with the TBO calibration curve at 632 nm. The morphology and size of TBO-GNPs were characterized using a transmission electron microscopy (FEI Tecnai G220 TEM). UV-vis absorption spectroscopy was performed using a Varian Cary spectrophotometer **(Figure 1a, b)**. Conjugation was observed to increase the molar extinction coefficient by 19% at the irradiation wavelength (632 nm) **(Figure 1b)**. The spectra obtained indicate a clear summation of the GNPs and TBO photosensitizer, implying that no new species were created in the chemical process. The red absorption band of TBO at peak 630 nm shows clear enhancement post-conjugation due to plasmon resonance absorption which occurred for the GNPs used due to their size, calculated from TEM as 10 ± 3.2 nm from a 120 GNP sample analysis **(Figure 1a)**.[20,21] TEM imaging of the particles also demonstrated uniform spherical morphology and good particle separation with no evidence of aggregation. FTIR analysis of GNPs, free TBO, and TBO-GNP conjugates provided good evidence for the effectiveness of the coupling reaction between AuNPs and TBO **(Figure S1)**. The peak at 1600 cm^{-1}, assigned to the aromatic rings of the TBO, is observed in the TBO-GNPs spectrum.

2.2 Cell culture

Human colon cancer cells (SW480) were cultured in maintenance medium consisting of Dulbecco's modified Eagle medium (DMEM) (Sigma –Aldrich, UK), 10% fetal bovine serum

(Sigma –Aldrich, UK) and 100 U/ml penicillin-streptomycin (Sigma-Aldrich, UK) at 37 ºC in a humidified atmosphere with 5% CO_2. For in vitro PDT experiments, SW480 cells were seeded into 96 cell culture well plate at cell density of 1×10^4 cells /ml and incubated for 24 hours. Various concentrations (0-1μM) of TBO-GNPs were added to the cells and incubated for 24 hours.

2.3 PDT treatment

After incubation, the cells were irradiated with different energy density doses (0, 6, 18, and 30 Jcm^{-2}) with a He-Ne laser at 632.8 nm. The cells were then incubated for a further 24 hours and the viability of cells was determined using a standard methyl thiazolyl tetrazolium (MTT) assay (Sigma-Aldrich, UK). Toxicity evaluation with this assay indicated that the conjugates were effectively non-toxic in the absence of light, even at a maximum concentration **(Figure 1c)**. The addition of GNPs alone caused no phototoxicity **(Figure 1d)** but conjugation increased phototoxicity by 98% as compared to free sensitizer **(Figure 1d)**. 35.8% of cells were rendered non-viable by free TBO treatment for these conditions (dark level-62.2%) whereas for conjugated TBO this increased to 71% (dark level-27%). As a fraction, this effectiveness can be described as an increase of (71-35.8)/35.8 = 98%. A high dosage applied to cells without particles was also completely non-toxic, whereas an energy dose of 30 Jcm^{-2} applied to the highest concentration TBO-GNPs (1μM) induced apoptosis in 93% of the culture. Cells for AFM analysis were cultured on cover slips as substrates for 24 hours. TBO-GNPs were added at 0.75 μM and incubated for another 24 hours and irradiated for 10 min at 30 Jcm^{-2}. Fixation was performed post PDT treatment with 3.7% paraformaldehyde for 10 min.

2.4 Apoptosis assessment

Evaluation of apoptotic and necrotic cell populations following PDT was performed using two methods, flow cytometry using Annexin-V-FITC/PI assay (BD Pharmingen™, San Diego, CA) and fluorescence microscopy using an acridine orange / propidium iodide dual stain assay (Sigma –Aldrich, UK). SW480 cells treated with TBO-GNPs (0.75μM) for 24 hours were then exposed to laser light for 10 min (30 Jcm^{-2}). The percentage of cells at different phases of cell death (live, early apoptosis, late apoptosis and dead cells) was quantified using a Cell Lab Quanta SC flow cytometer (Beckman Coulter, USA) and analyzed using FlowJO software. Flow cytometry indicated a 28% increase in early and 32% increase in late stage apoptosis post treatment as compared with the control (Figure 1e). This was in good agreement with characterization by fluorescence microscopy which indicated 32% viable and 68% apoptotic cells after PDT (Figure 1f).

2.5 AFM measurements

Topographic and force analysis was performed using an AFM (Veeco Explorer, CA, USA) in conventional contact mode in order to image and assess cell deformation, attachment and morphology at a subcellular scale. Silicon nitride tips with nominal lengths of 120 microns mounted on V-shaped cantilevers (Bruker, Coventry, UK) with 0.05-0.5 N/m nominal spring constants were used. Force set-points between 0.5-2 nN were employed with typical scan speeds of 0.5 - 2 Hz and with pixel sizes ranging from 10-50 nm for roughness measurements and 100-300 nm for volume measurements. These corresponded to scan sizes in the range of 300-500 pixels for both roughness and volume measurements, although at an order of magnitude different length scales. Faster imaging was unreliable given the scan sizes used for full cell imaging, typically 60x60 μm^2 to 80x80 μm^2 in air. Inaccuracies emerged in the volume calculation if scanning conditions above 500 nm/pixel were used. Previous studies of soft matter using these

experimental conditions yielded resolvable features below 50 nm.[22-25] Images were sampled from the population at random. However, multiple locations several millimeters apart were always chosen in order to optimally represent the population and to avoid spatially dependent local errors (e.g. local substrate or chemical characteristics). No outlier criterion was applied to the images processed, but only images showing the entirety of the cell boundary were used, as otherwise this would always under-represent cell volume.

2.6 Image processing and Data analysis

AFM image processing was performed using the Gwyddion™ software package. Data analysis for the volume and roughness was performed by importing images into MatLab™ after conversion to ASCII format. All images were acquired in contact mode, levelled using 3-point background subtraction and cropped to the cell boundary in order to minimize errors that would occur due to the excess inclusion of the substrate. The influence of pixel density was determined to be very low (<1%) by volume calculation of low resolution (1μm/pixel) images. Cell volume is the integral of height over each point of the cell surface area. Given a $m \times n$ pixel scan, this was calculated as the summation of the z-height, z for every pixel, divided by the pixel density per μm^2, d.

$$V = \sum_{i=1}^{m \times n} z_i / d$$

A variety of mathematical approaches can be employed to measure roughness, although the root mean square approach is popular for AFM analysis of cells as it is preferably influenced by large morphological defects and intuitively approximates a measure of surface ruggedness. The mean surface roughness value, R_{rms} was calculated as the root mean square of the height distribution difference from the mean height.[26] Several parameters affect the roughness value obtained from

AFM images, these include sampling density, image size, scan speed, number of data points obtained, the level of force applied and the probe geometry. Typical cell surface roughness values using the R_{rms} approach are known to range from 100 nm to 800 nm.

Since the roughness also depends on the sampling size, two different areas of cell membrane were chosen from each cell at random for the roughness estimation. Previous studies[15] have indicated that the experimental error due to single variables is around 2%, although the multiple variables which influence roughness are likely to lead to a larger net error.

3. Results and Discussion

3.1 Characterization and PDT effects of TBO-GNPs

Here we outline how apoptosis initiated by PDT using photosensitizer conjugated gold nanoparticles mediates the morphological properties of single colon cancer cells. We describe a bivariate morphological measurement based on AFM of single cells which is an efficient classifier of cell health and a competitive method for detecting apoptosis.

Characterization studies of the TBO-GNPs conjugates illustrated well formed, spherical non-aggregated nanoparticles **(Figure 1a)** with only minimal toxicity pre irradiation which, after irradiation, induced a high level of cell death as compared with the free sensitizer **(Figure 1c, d)**. Flow cytometric and fluorescence microscopy analysis **(Figure 1e, f)** for control and post PDT samples illustrated that apoptosis was the primary mechanism of cell death. This is consistent with previous studies which interrogate the pathways of cell death induced by PDT, which typically demonstrate high levels of apoptosis.[27-30]

3.2 Morphological features of Apoptotic cells

The sequential biochemical pathways which occur in early stage apoptosis induce a variety of characteristic morphological cell changes when compared to control cells **(Figure S2)**, these ranges in size from the extremely subcellular scale up to the whole cell length scale, such as in **Figure 2a**, which illustrates numerous morphological features of apoptosis.[31] Although the majority of these features can be observed with appropriate use of fluorescence stains,[32] AFM imaging provides many advantages due to its resolution and method of detection, including three dimensional nanoscale quantification of hole and pore formation **(Figure 2b)**, nuclear condensation and fragmentation **(Figure 2c)**, the excretion of intact vesicles **(Figure 2d)**, blebbing of the membrane and changes to surface roughness **(Figure 2e)**.

However, not all apoptotic cells were observed to excrete large apoptotic bodies, and the highest point in a cell's surface does not necessarily indicate the nucleus, or fragments thereof, but may simply be another morphological feature such as a clustering of organelle mass. Therefore although these features are characteristic of apoptosis, they are unreliable for classifying all cells. Unlike the other physical changes listed above, cell volume and surface roughness are quantities measurable irrespective of cell state. Hence roughness and volume were our preferred morphological features of interest. Literature demonstrates many precedents for using AFM analysis for these quantities, which are directly known to be mediated by apoptosis; further, the relative experimental ease and processing simplicity with which they can be obtained makes them the ideal bivariate morphological measurement of apoptosis.[33,34]

3.3 Morphological variables for viable and apoptotic cells

In fact, our observations indicated that no choice of single variable was capable of discriminating apoptosis for small numbers of cells and that neither cell volume nor roughness alone was always a reliable discriminant of apoptosis. This is because the inherent cell to cell variation in size and roughness is also influenced by factors other than the state of cell health. For example, the cell cycle mediates cell volume. It is also known that cell roughness is influenced by several environmental and subcellular state factors such as motility, adhesion, and intracellular contact is therefore a good indicator of cell health.[35] **Figure 3** shows the variance of roughness and volume for two viable and two apoptotic cells. Volumetric assessment of cell shrinkage as shown in **Figure 3a-d** indicated both large and small volumes were present in both the control and post treatment samples. Similarly, the inherent variation in membrane roughness **(Figure 3e-h)** was large compared to the difference between the population means. Additionally, even within the same cell, roughness calculation based on different subcellular areas indicated nearly 20% inherent variation in the measurement **(Figure 4)**.

Therefore although AFM enables ultra-high resolution imaging of morphological features, our results indicated that single cell and single parameter analysis does not robustly reflect culture population dynamics. This clearly demonstrates a lack of specificity and selectivity in singular measurements of morphology for small cell numbers; as we would expect, this inherent morphological variation becomes pronounced when cell selection is randomized. Therefore, true mechanical discrimination creates a compelling need for multivariate morphological analysis, which clearly must be assessed with a larger sample size.

The bar chart in **Figure 4b** shows that in contrast to the low cell number study outlined in **Figure 2**, there is a consistent underlying difference in the averages obtained for the roughness and volume between the viable (control, blue bars) and the apoptotic cells (post-PDT, red bars) for

larger samples, in this case 100 cells. Both volume and roughness discriminate control and post-treatment populations with $p < 0.0001$; however, neither measurement accurately classified all cells unlike fluorescence microscopic analysis. Therefore, although single variable analysis permitted separation of the two populations, it was unable to classify individual cells with the same accuracy due to inherent variation in either variable. However, when taken together, a cell is statistically far less probable to display both a volume atypical of its state and a roughness atypical of its true state. Hence, a multivariate analysis was performed, however subtleties exist in this analysis, and we now provide a detailed discussion of the relevant bivariate distribution properties of cell morphological indicators.

3.4 Bivariate analysis

The typical distribution type of human cell volume is known; and as with the empirically observed volume distribution of a wide variety of cells, it is composed of a primary Gaussian distribution summed with one sided exponential decay curves.[36] However, the average cell size in a culture is time dependent and is strongly influenced by the mean cycle stage of the population. Classification and omission of highly atypical cells and cells during mitosis (especially post metaphase) was required for bivariate analysis as they would negatively skew the distribution or create excess outliers atypical of the density function, i.e., not Gaussian. Previous analysis of the volume reduction which occurs during apoptosis using AFM indicated only the mean reduction to the sample observed and the reduction of single cell volume as a function of time.[33] However, apoptosis occurs only at particular checkpoints in the cell cycle, which constitutes further evidence that other morphological characteristics, such as membrane

roughness are more likely to act as robust discriminants of apoptosis than volume measurements alone.[37]

An assumption about the distribution of cell roughness was also required for fitting. The distribution of cellular surface roughness is less certain, however, as it is co-dependent on many factors, a situation which is further complicated by the fact that the distribution type of cell roughness on the nanoscale has not been previously classified. Positively skewed distributions commonly observed in biology are often approximated with gamma or lognormal functions, although exponentially modified Gaussians are also known to be effective for describing cell properties. For this study, the difference in least squares fit of gamma, lognormal and Gaussian functions was small for roughness measurements, and so the dataset was assumed to be Gaussian for ease of analysis. This was justified by the strong fit between empirical and theoretical Gaussian cumulative distribution functions for the volume **(Figure 5a)** and roughness **(Figure 5b)**.

Bivariate Gaussians were fitted to the roughness and volume data of both control and post-treatment populations. A 2D plot showing the viable and control distribution is shown in **(Figure 5c)**. The control-fitted Gaussian and post-treatment Gaussian distributions are shown to the 3σ (i.e. 99.7%) boundary by color coded shaded areas. Using the 3σ boundary as a reasonable choice of cut-off (giving an expected error of ca. one cell) showed that 20% of the post treatment cells were still viable, i.e. within the control distribution area. These cells are illustrated in **(Figure 5c)** by red circles with a white interior. This number of viable cells is in excellent agreement with the flow cytometry data which indicated that 21% of the post treatment cells were still viable. However, it is noted that a simple multinomial test indicated that a deviation of 5% in the viable percentage would not be uncommon given the sample size used.

Looking at a subsection of the 2D distribution plot in detail, there are many examples where a single variable morphological assessment would have indicated an incorrect classification, despite the fact that as shown in **Fig. 3b**, the overall distributions are well separated by either measurement. In **Figure 5d** the volume change is very small between two cells, and they both appear to fall within the control distribution. However, the roughness difference between them allows the two cells to be separated. In this case, the red point indicates that the cell, after treatment remains viable. Similarly, in **Figure 6e** the change in volume greatly outweighs the change in roughness. If only roughness was measured, both cells would be considered viable; however, the significant loss in volume of the red post-treatment cell indicates that it is outside the 2D Gaussian viable region boundary. Therefore, combining both measurements greatly improves classification accuracy, and represents a significant advance on previous single variable AFM cell morphology studies.

We highlight the ability of the bivariate AFM classification method described here to robustly classify population health by comparing the results obtained from **Figure 5b** with both of the current biological standards for apoptotic detection; fluorescence microscopy and flow cytometry **(Figure 6)**. No significant differences were observed between the percentages obtained by the three methods.

Conclusion

Previous AFM imaging studies of apoptotic cells have indicated both increased and decreased membrane roughness after various treatments. Here, we have shown a consistent and significant decrease in membrane roughness of cells undergoing apoptosis induced by photodynamic therapy. However, 14% of the post treatment cells had roughness parameters within the limits of the control distribution. Additionally, even within a single cell, a roughness calculation based on

different subcellular areas indicated nearly 20% inherent variation in the measurement, which significantly reduces the sensitivity of roughness as a measure of cell health. Therefore although AFM enables ultrahigh-resolution imaging of morphological features, our results indicated that single cell and single parameter analysis does not robustly reflect culture population dynamics. Therefore, we cross confirmed our results from AFM analysis of membrane roughness with a previously described volume measurement methodology on a cell-by-cell basis.

Bivariate Gaussian fitting of these two independent parameters allowed the discrimination of viable and apoptotic populations, even in several cases where a single morphological variable assessment alone would have led to inaccurate classification of individual cells. The robustness of this method, however, should be further interrogated for a range of cell lines. Therefore, when multiparameter measurements are taken for a large number of cells, we illustrate that AFM provides a highly competitive method for determining apoptosis, with comparable identification accuracy to both of the current biological standards for apoptotic detection: fluorescence microscopy and flow cytometry. This work indicates that provided certain experimental constraints are met, AFM is not only a useful method for detecting subtle structural changes that occur with photodynamic therapy, but it can also provide a useful measure of cell health, provided the morphological parameters mediated by apoptosis are measured in combination.

Acknowledgments

This work was funded by Science Foundation Ireland (SFI). This research was co-funded by the Islamic development bank and the Ministry of Higher Education and Scientific Research of Iraq.

AUTHOR CONTRIBUTION

R.A.M., E.K. conducted experiments and analyzed data. M.A.R., J.H.R. and D.Z. analyzed and interpreted the data. R.A.M., E.K. and D.Z. wrote the manuscript. All authors discussed and commented on the manuscript.

COMPETING FINANCIAL INTERESTS

The authors declare no competing financial interests.

REFERENCES

1. M. Al-Rubeai and R. P. Singh, *Current Opinion in Biotechnology*, 1998, **9**, 152-156.
2. M. Al-Rubeai, in *Bioprocess and Algae Reactor Technology, Apoptosis*, Springer Berlin Heidelberg, 1998, vol. 59, ch. 6, pp. 225-249.
3. H. U. Simon, A. Haj-Yehia and F. Levi-Schaffer, *Apoptosis*, 2000, **5**, 415-418.
4. M. L. Circu and T. Y. Aw, *Free Radical Biology and Medicine*, 2010, **48**, 749-762.
5. D. E. J. G. J. Dolmans, D. Fukumura and R. K. Jain, *Nat Rev Cancer*, 2003, **3**, 380-387.
6. N. L. Oleinick, R. L. Morris and I. Belichenko, *Photochemical & Photobiological Sciences*, 2002, **1**, 1-21.
7. E. Buytaert, M. Dewaele and P. Agostinis, *Biochimica et Biophysica Acta (BBA) - Reviews on Cancer*, 2007, **1776**, 86-107.
8. S. Gupta, B. S. Dwarakanath, K. Muralidhar and V. Jain, *Journal of Photochemistry and Photobiology B: Biology*, 2003, **69**, 107-120.
9. S.-H. Jung, J.-Y. Park, J.-O. Yoo, I. Shin, Y.-M. Kim and K.-S. Ha, *Ultramicroscopy*, 2009, **109**, 1428-1434.
10. H. Jin, P. Yang, J. Cai, J. Wang and M. Liu, *Applied microbiology and biotechnology*, 2012, **94**, 1199-1208.
11. M. Al-Rubeai, S. H. G. Khoo, R. P. Singh and M. C. Flickinger, in *Encyclopedia of Industrial Biotechnology*, John Wiley & Sons, Inc., 2009, DOI: 10.1002/9780470054581.eib055.
12. V. Shahin and N. P. Barrera, *International review of cytology*, 2008, **265**, 227-252.

13. A. Alessandrini and P. Facci, *Measurement science and technology*, 2005, **16**, R65.
14. M. Hu, J. Wang, H. Zhao, S. Dong and J. Cai, *Journal of Biomechanics*, 2009, **42**, 1513-1519.
15. K. S. Kim, C. H. Cho, E. K. Park, M.-H. Jung, K.-S. Yoon and H.-K. Park, *PLoS ONE*, 2012, **7**, e30066.
16. H. Jin, X. Zhong, Z. Wang, X. Huang, H. Ye, S. Ma, Y. Chen and J. Cai, *Journal of Cellular Biochemistry*, 2011, **112**, 169-178.
17. H. Jin, H. Zhao, L. Liu, J. Jiang, X. Wang, S. Ma and J. Cai, *Scanning*, 2013, **35**, 7-11.
18. M. Brust, M. Walker, D. Bethell, D. J. Schiffrin and R. Whyman, *Journal of the Chemical Society, Chemical Communications*, 1994, DOI: 10.1039/c39940000801, 801-802.
19. Y. Liu, M. K. Shipton, J. Ryan, E. D. Kaufman, S. Franzen and D. L. Feldheim, *Analytical chemistry*, 2007, **79**, 2221-2229.
20. G. Doyle, B. Ashall, M. Galvin, M. Berndt, S. Crosbie and D. Zerulla, *Applied Physics A*, 2007, **89 (2)**, 351-355.
21. C. Andrei, E. Lestini, S. Crosbie, C. de Frein, T. O'Reilly and D. Zerulla, *PLoS ONE,* 2014, **9(10)**: e109836. (doi:10.1371/journal.pone.0109836)
22. Z. E. Mousavi, E. Kennedy, S. Fanning, J. H. Rice and F. Butler, *Food Control*, 2014, **42**, 277-283.
23. E. Kennedy, F. Yarrow and J. H. Rice, *Journal of biophotonics*, 2011, **4**, 588-591.
24. E. Kennedy, R. Al-Majmaie, M. Al-Rubeai, D. Zerulla and J. H. Rice, *RSC Advances*, 2013, **3**, 13789-13795.
25. E. Kennedy, R. Al-Majmaie, M. Al-Rubeai, D. Zerulla and J. H. Rice, *Journal of biophotonics*, 2015, **8**, 133-141.
26. M. Girasole, G. Pompeo, A. Cricenti, A. Congiu-Castellano, F. Andreola, A. Serafino, B. Frazer, G. Boumis and G. Amiconi, *Biochimica et Biophysica Acta (BBA)-Biomembranes*, 2007, **1768**, 1268-1276.
27. D. Kessel and Y. Luo, *Cell Death and Differentiation*, 1999, **6**, 28-35.
28. S. M. Ali, S. K. Chee, G. Y. Yuen and M. Olivo, *International journal of molecular medicine*, 2002, **9**, 257-270.
29. R. Wu, C. Yow, C. Wong and Y. Lam, *Photodiagnosis and photodynamic therapy*, 2011, **8**, 254-263.

30. P. Mroz, A. Yaroslavsky, G. B. Kharkwal and M. R. Hamblin, *Cancers*, 2011, **3**, 2516-2539.
31. G. Häcker, *Cell and tissue research*, 2000, **301**, 5-17.
32. S. Elmore, *Toxicologic pathology*, 2007, **35**, 495-516.
33. D.-C. Wang, K.-Y. Chen, C.-H. Tsai, G.-Y. Chen and C.-H. Chen, *Journal of Biomechanics*, 2011, **44**, 2790-2794.
34. J. A. Hessler, A. Budor, K. Putchakayala, A. Mecke, D. Rieger, M. M. Banaszak Holl, B. G. Orr, A. Bielinska, J. Beals and J. Baker, *Langmuir*, 2005, **21**, 9280-9286.
35. A. E. Pelling, F. S. Veraitch, C. P. K. Chu, C. Mason and M. A. Horton, *Cell motility and the cytoskeleton*, 2009, **66**, 409-422.
36. E. H. Chapman, A. S. Kurec and F. Davey, *Journal of clinical pathology*, 1981, **34**, 1083-1090.
37. B. Krampe and M. Al-Rubeai, *Cytotechnology*, 2010, **62**, 175-188.

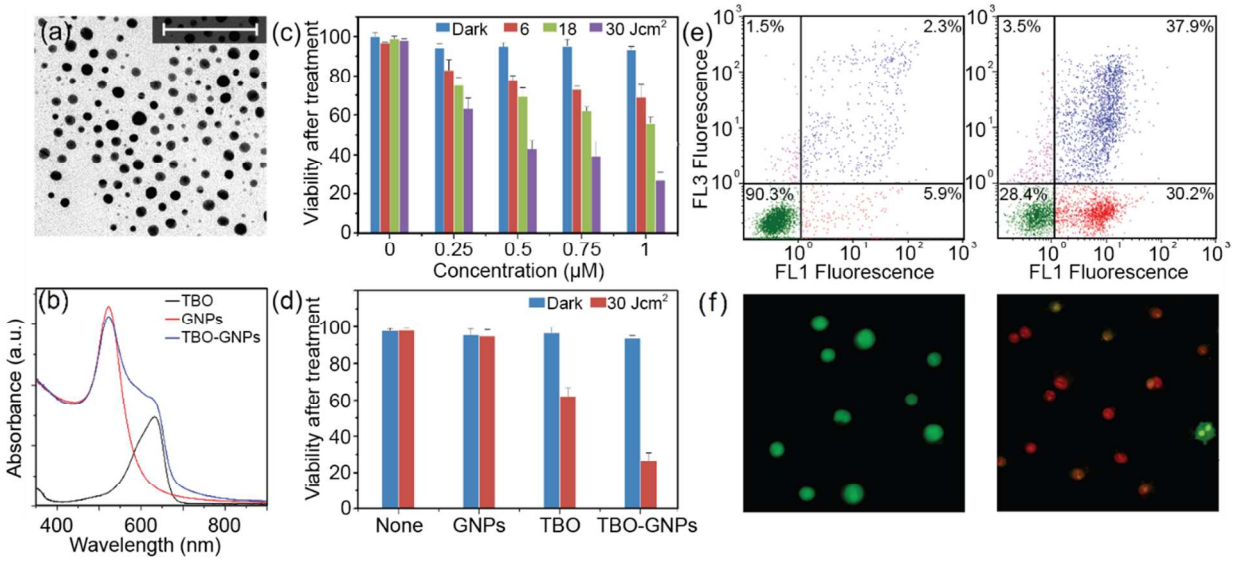

Figure 1: Characterization, cytotoxicity of TBO-GNPs and PDT mediated induction of apoptosis. (a) TEM image of TBO-GNPs. The scale bar is 100 nm. **(b)** Absorption spectra of free TBO (black), GNPs (red) and TBO-GNP conjugates in distilled water. **(c)** PDT cytotoxicity of TBO-GNPs with different concentrations in SW480 cells for four light doses with He-Ne laser

at 632.8 nm, 0 Jcm^{-2} (Dark), 6 Jcm^{-2}, 18 Jcm^{-2} and 30 Jcm^{-2}, as determined by the MTT assay. **(d)** SW480 cell viability following incubation with free GNPs, free TBO and TBO-GNP conjugates (0.75µM) for 24 hours and subsequent irradiation (30 Jcm^{-2}). **(e)** Flow cytometric analysis for control **(left)** and post PDT **(right)** samples with PI and Annexin V. **(f)** Measurement of apoptosis by fluorescence microscopy was carried out using acridine orange/ propidium iodide dual staining assay for control **(left)** and post-PDT **(right)** cells. The cells were treated with 0.75 µM TBO-GNPs at light dose 30 Jcm^{-2} and analyzed 16 hours after treatment which illustrated a significant increase in the percentage of apoptotic cells post-irradiation.

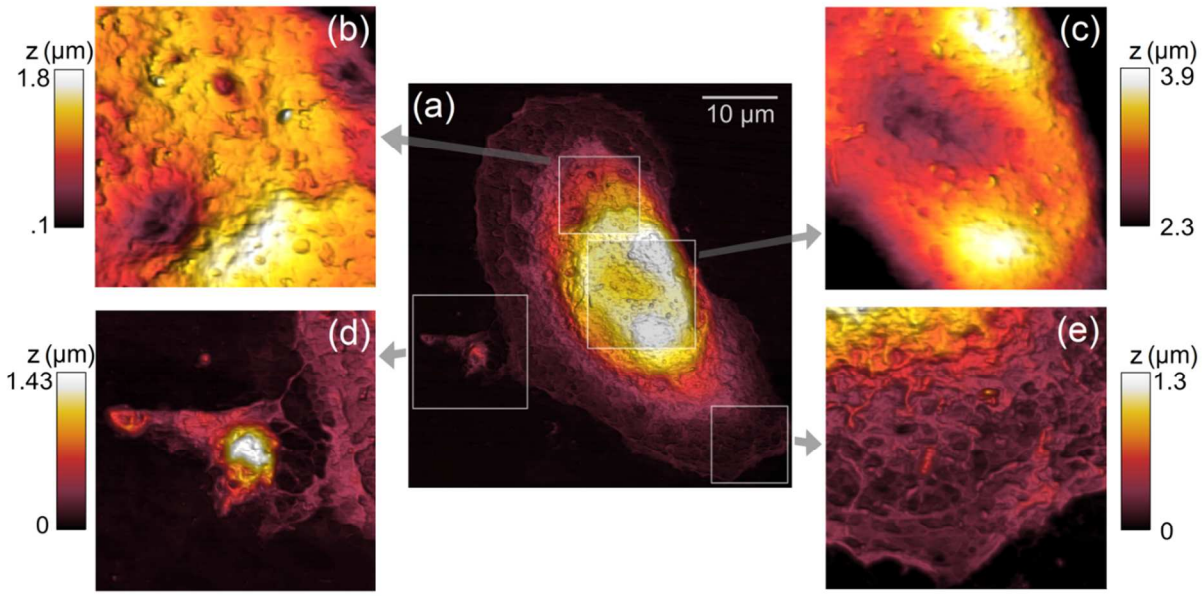

Figure 2: Morphological evidence of apoptosis. AFM imaging of a typical apoptotic cell **(a)** permits three dimensional quantification of apoptosis-driven morphological changes which are known to include hole and pore formation **(b)**, nuclear condensation and fragmentation **(c)**, the excretion of apoptotic bodies **(d)** and zeiotic formation at the cell boundary which occurs in combination with changes in membrane roughness **(e)**. All heights are color coded in µm, although with varying z maxima as shown.

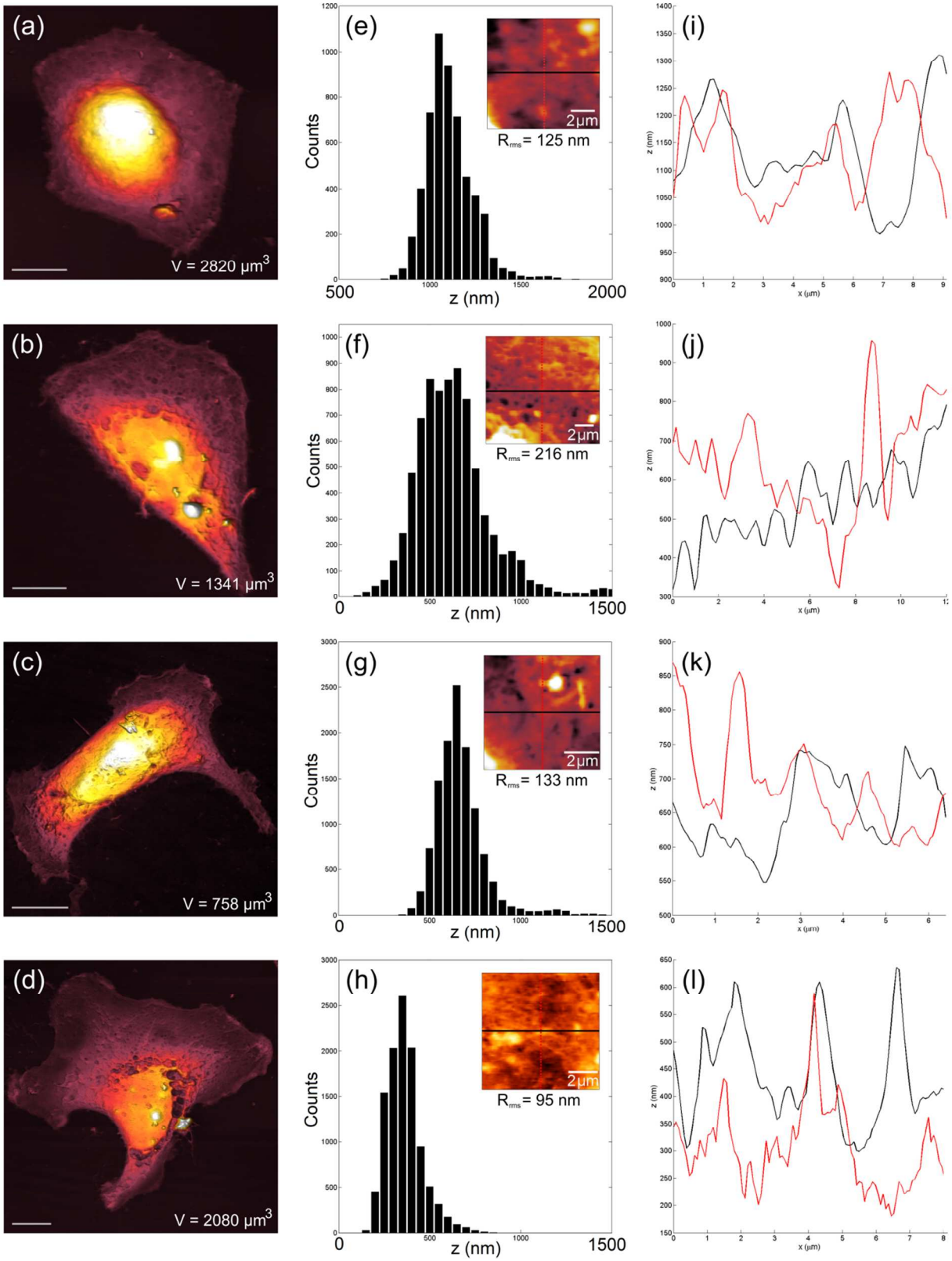

Figure 3: Population variance of morphological variables for viable and apoptotic cells. Volumetric assessment of cell shrinkage as shown in **(a) – (d)** and membrane roughness, calculated from the roughness distributions **(e) – (h)** and roughness line profiles **(i) – (l)** by AFM. We observed large ranges for volume and roughness in both the control **(a, b, e, f, I,** and **j)** and post PDT **(c, d, g, h, k**, and **l)** samples. The inherent population variance for either single variable assessment of apoptosis is large compared to the difference between the population means. This illustrates the need for multivariate morphological analysis, which clearly must be assessed with a larger sample size.

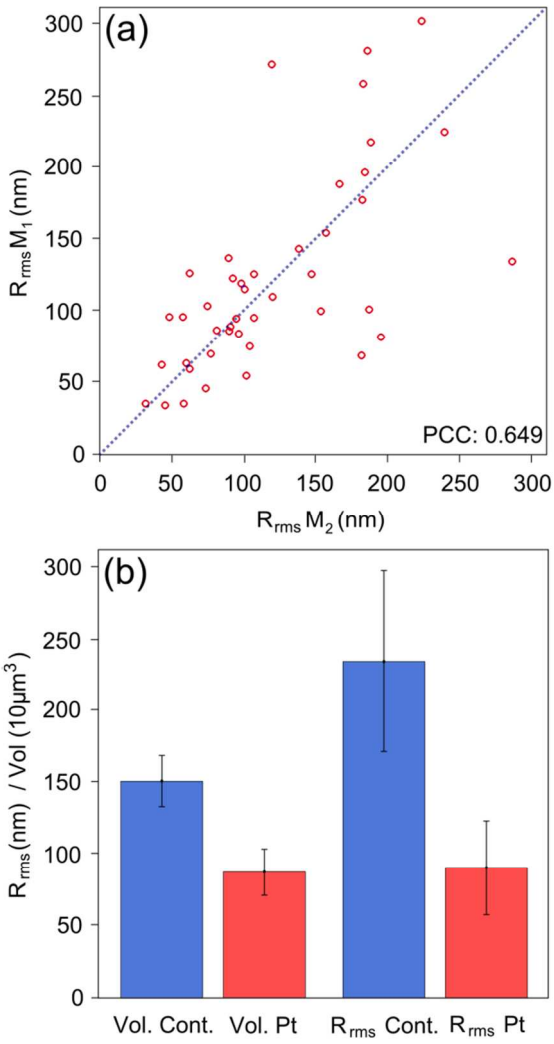

Figure 4: Choice of cell subsection analyzed and average values obtained. Two cell subsections were chosen at random from each apoptotic cell; the two R_{rms} subsection values found for each cell are plotted against each other in **(a)**. Although there were isolated cases of poor fit, generally good one-to-one agreement (blue dotted line) was observed, which indicates no bias or trend in the choice of subsection analyzed. The bar chart in **(b)** shows that, in contrast to the low cell number study outlined in Figure 3, a consistent underlying difference exists in the averages obtained for the roughness and volume between the viable (control - blue bars) and the apoptotic cells (post-PDT - red bars) for larger samples (n > 100).

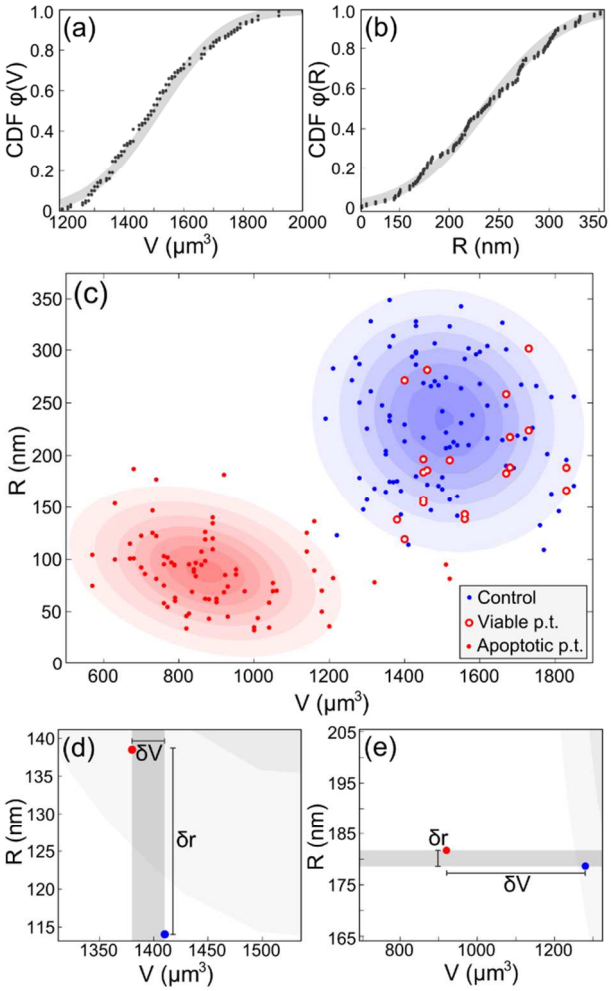

Figure 5: Bivariate Gaussian approximation of morphology of viable and apoptotic cells. Cumulative distribution functions for the volume **(a)** and roughness **(b)** showed good agreement with a theoretical Gaussian fit. Additionally the choice of fit type did not significantly change results, so normality was assumed for both variables. A 2D plot showing the viable and control distribution is shown in **(c)**. The control-fitted Gaussian (blue shaded) and post-treatment Gaussian (red shaded) distributions are shown to the 3σ boundary. Using this as a reasonable choice of cut-off (giving an expected error of ca. one cell) showed that 20% of the post treatment cells were still viable, i.e. within the control distribution. These cells are illustrated in **(c)** by red circles with a white interior. In **(d)** the volume change (δV) is very small between two cells, but

the roughness difference between them (δr) allows the cell to be classified within the correct distribution boundary. Similarly in **(e)** the change in volume greatly outweighs the change in roughness which only in combination allows for correct classification - in this case, discriminating a viable from an apoptotic cell.

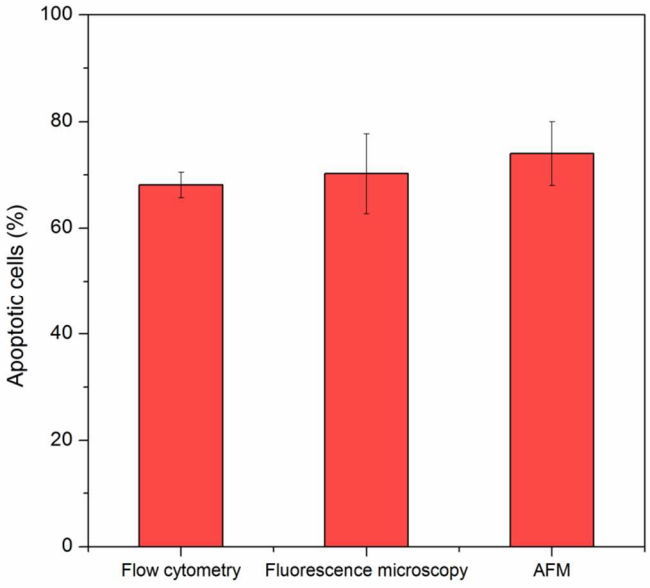

Figure 6: Apoptosis assessment using flow cytometry, fluorescence microscopy and AFM.

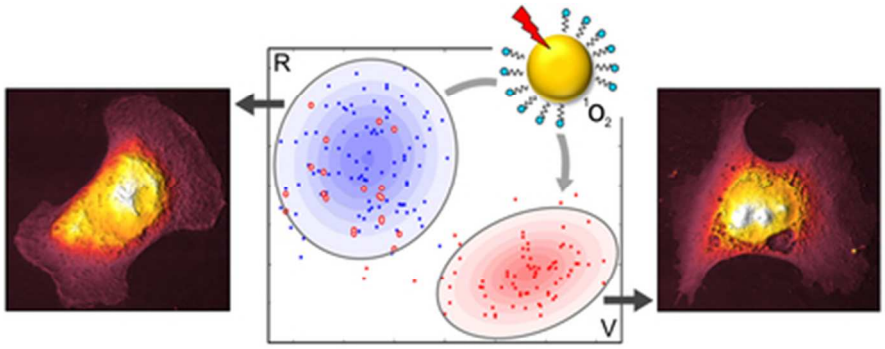

Typical examples of the morphology of one viable and one apoptotic cell together with the statistical analysis of a larger cell ensemble subsequent to photodynamic treatment.
37x15mm (300 x 300 DPI)